# Unravelling the free electron behavior in InN

V. Darakchieva*† T. Hofmann‡, M. Schubert‡, B.E. Sernelius†, F. Giuliani†, M.-Y. Xie†,
P.O.Å. Persson†, B. Monemar†, W. J. Schaff§, C.-L. Hsiao¶, L.-C. Chen¶, and Y. Nanishi‖
*Instituto Technológico e Nuclear, 2686-953 Sacavém, Portugal
†Department of Physics, Chemistry and Biology, Linköping University
SE-58183 Linköping, Sweden
Email: vanya@itn.pt, vanya@ifm.liu.se
‡Department of Electrical Engineering and Nebraska Center for Materials and Nanoscience,
University of Nebraska-Lincoln, NE 68588, U.S.A.
§Department of Electrical and Computer Engineering, Cornell University, Ithaca, NY 14853, U.S.A.
¶Center for Condensed Matter Sciences, National Taiwan University, Taipei 106, Taiwan
‖Department of Photonics, Ritsumeikan University, Shiga 525-8577, Japan

*Abstract*— **Precise measurement of the optical Hall effect in InN using magneto-optical generalized ellipsometry at IR and THz wavelengths, allows us to decouple the surface accumulation and bulk electron densities in InN films by non-contact optical means and further to precisely measure the effective mass and mobilities for polarizations parallel and perpendicular to the optical axis. Studies of InN films with different thicknesses, free electron densities and surface orientations enable an intricate picture of InN free electron properties to emerge. Striking findings on the scaling factors of the bulk electron densities with film thickness further supported by transmission electron microscopy point to an additional thickness dependent doping mechanism unrelated to dislocations. Surface electron accumulation is observed to occur not only at polar but also at non-polar and semi-polar wurtzite InN, and zinc blende InN surfaces. The persistent surface electron density shows a complex behavior with bulk density and surface orientation. This behavior might be exploited for tuning the surface charge in InN.**

## I. Introduction

Recent developments in group-III nitride technology have led to the commercialization of variety of optoelectronic devices with large impact on everyday life. In particular, high-brightness blue and white light emitting diodes based on InGaN promise more efficient lighting solutions [1]. An emerging potential application of InGaN and InAlN alloys is in highly efficient multijunction solar cells [2] addressing the immediate need of developing sustainable renewable energy sources. Furthermore, InN and related alloys are promising for developing high-frequency transistors, THz emitters and chemical sensors. Driven by the attractive material applications, the epitaxial techniques to grow InN and related alloys have made significant advances and matured during the last decade. However, our poor understanding of the doping mechanism in InN and related alloys is one of the critical issues that hinder further progress in the InN based technology towards full exploitation of the material potential.

Understanding and controlling doping mechanisms in semiconductors are indispensable for their incorporation into new electronic devices, and challenge scientists to unravel the physics behind the sometimes peculiar free-charge carrier generating mechanisms. As a result of its exceptional propensity for *n*-type doping [3] all unintentionally doped InN is *n*-type conductive but the exact doping mechanism is under debate [4]–[6]. Particular difficulties to assess doping in InN and In rich alloys are encountered because of the presence of electron accumulation at the film surfaces. Electrical measurements are dominated by the accumulation layer conductivity, complicating their interpretation, since the exact current paths are difficult to determine. The latter are required in order to assign separately the free-charge carrier densities and mobilities to the individual constituents of a layered sample. Further *p*-type conductivity will be obscured by the surface electron accumulation in a single Hall effect measurement. Recently, electrolyte capacitance-voltage and Hall effect measurements at variable magnetic fields combined with photoluminescence have provided evidence for *p*-type doping in Mg-doped InN films [7], [8]. Although these techniques offer access to some of the free-charge carrier properties of either the surface or the bulk of *n*- and *p*-type InN films, separate and unambiguous quantitative assignment of surface and bulk carrier mobility, density, effective mass and sign has not been achieved yet. This entanglement of surface accumulation and bulk charge densities in InN hinders the development of a better understanding of the doping mechanisms in the material and the assessment of the impact of dopants.

Likewise, considerable efforts have been focused on understanding the microscopic origin and nature of the electron accumulation at InN surfaces [9]–[11]. Most experimental work on the surface electron accumulation has been concentrated on wurtzite (WZ) (0001)-oriented (*c*-plane) InN [9], [10], [12], [13]. The electron accumulation was observed at the (0001) surfaces of WZ InN and suggested to be a consequence of the low $\Gamma$ point conduction band minimum (CBM) of the material (lying significantly below the charge neutrality level) [9], [10]. The electron accumulation at the polar InN surfaces was explained by the presence of occupied In-In bond surface states above the CBM [11]. Recently, the growth of WZ non-polar, semi-polar and zinc-blende (ZB) nitrides has become of significant technological importance, since it offers a promising approach to overcome the deteriorating

effects of the built-in electric fields on variety of device-relevant characteristics of the materials [14]–[16]. Recent theoretical studies have predicted presence or absence of electron accumulation at nonpolar InN surfaces depending on In/N ratio and surface reconstruction [11]. The presence of electron accumulation at the surfaces of WZ $(11\bar{2}0)$- and ZB (001)-oriented InN has been inferred on the basis of X-ray photoemission spectroscopy (XPS) studies [17], and at the nonpolar surfaces of InN nanocolumns by Raman scattering spectroscopy [18].

In this work we report a comprehensive study of the free electron behavior in InN films with different crystal modifications, surface orientations, and bulk carrier densities. We first demonstrate the disentanglement of the bulk and surface free charge carrier properties in *c*-plane InN thin films through the optical Hall effect, which allows us to explore the trends in the true bulk and surface accumulation electron densities. We further report on the free electron properties in ZB (001)- and WZ $(11\bar{2}0)$-, and $(10\bar{1}1)$-oriented InN thin films using generalized infrared spectroscopic ellipsometry (GIRSE), evidencing distant accumulation of electrons at their surfaces.

## II. Experimental and modeling

InN samples with different surface orientations were grown by molecular beam epitaxy (MBE). A series of unintentionally doped *n*-type WZ InN films of different thickness from about 550 to 1600 nm and a 500 nm thick Si-doped InN film, all with *c*-plane (0001) orienatation were studied by the optical Hall effect. These (0001) InN films are grown on *c*-plane sapphire employing AlN and GaN nucleation layer sequences [19]. Next, ZB (001)- and WZ $(10\bar{1}1)$- and $(11\bar{2}0)$-oriented InN films with similar thicknesses of about 400 - 500 nm were studied by GIRSE. In this case the growth was realized on $(1\bar{1}02)$ sapphire substrates without a buffer layer and employing nitridation pre-treatment of the substrates [20], [21]. Different crystal modifications and film orientations were achieved by carefully controlling the nitridation time [20], [21].

The crystal structure and film orientation was determined by high-resolution x-ray diffraction using a Philips X'pert triple axis diffractometer [22]. The purity of the ZB phase was carefully examined by reciprocal space mapping around the ZB (001) reciprocal space point at the four $\{111\}$ azimuths and estimated to be about 75%. All InN films exhibit *n*-type conductivity as measured by standard single field electrical Hall effect.

The free electron properties of the InN films were studied by optical Hall effect and GIRSE. The measurement of the optical Hall effect employs the use of magneto-optical generalized ellipsometry (MOGE) at infrared and THz wavelengths [23]. It allows precise and independent determination of the carrier type, density, mobility, and effective mass, and their distribution within individual layers of semiconductor heterostructures, providing equivalent and even increased information compared to the classical electrical Hall effect [23]–[28]. This new method does not require contacts in contrast to electrical capacitance, current and Hall effect measurements, and it is thus ideally suited for studying free charge carriers in InN heterostructures.

Both the Mueller matrix descriptor system and the Jones matrix formalism were used to describe the polarized response of the sample in the optical Hall effect and zero-field GIRSE measurements. The Mueller matrix connects the Stokes vectors, which describe the general polarization states before ($\mathbf{S}_{in}$) and after ($\mathbf{S}_{out}$) light interaction with the sample: $\mathbf{S}_{out}$=$\mathbf{M}\mathbf{S}_{in}$, where the elements $M_{ij}$, (*i*,*j*=1...4) are usually normalized to $M_{11}$. In the Jones matrix formalism the generalized ellipsometry parameters are described by three ratios of the polarized-light reflection coefficients among the four available complex-valued elements of the Jones reflection matrix $\mathbf{r}$ [29]–[32]. The ratios defining the generalized ellipsometry parameters $\Psi_{ij}$, $\Delta_{ij}$ are [29]:

$$\begin{aligned} \tfrac{r_{pp}}{r_{ss}} &\equiv R_{pp} = \tan\Psi_{pp}\exp(i\Delta_{pp}), \\ \tfrac{r_{ps}}{r_{pp}} &\equiv R_{ps} = \tan\Psi_{ps}\exp(i\Delta_{ps}), \\ \tfrac{r_{sp}}{r_{ss}} &\equiv R_{sp} = \tan\Psi_{sp}\exp(i\Delta_{sp}), \end{aligned} \tag{1}$$

and which depend on the layer sequence, layer dielectric function (DF), the relative orientation of the optical axis of the anisotropic material, and the layer thickness of each single constituent in a multi-layer structure.

Field-free (standard) GIRSE $\Psi$- and $\Delta$-spectra of all samples were collected at $\Phi$=70° and $\Phi$=60° angles of incidence. IR-MOGE experiments were carried out at $\Phi$= 45 ° with samples exposed to fields $\mu_0 H = +4.5$ T and $\mu_0 H = -4.5$ T. Model calculations, which account for the layered structure of the sample, are used to obtain information on the DF spectra, thickness, and relative optical axis orientation.

In the infrared and THz spectral region the DF $\varepsilon_j(\omega)$ is sensitive to phonon and plasmon effects. The infrared model DF can be written as a sum of lattice, $\varepsilon_j^L(\omega)$ and free-charge carrier, $\varepsilon_j^{FC}(\omega)$ contributions:

$$\varepsilon_j^L(\omega) \;=\; \varepsilon_j^L + \varepsilon_j^{FC}, \tag{2}$$

where the subscript "$j$" refers to the polarizability along the crystal principal axes.

A product-representation for harmonic oscillator lineshapes with Lorentzian broadening is employed for the calculation of the lattice contribution $\varepsilon^L$ to the DF of uniaxial crystals, such as wurtzite-structure group-III nitrides [23], [30]–[32].

The contribution from free-carriers to the dielectric functions at zero magnetic field is accounted for by the classical Drude model [31]–[33]:

$$\varepsilon_j^{(FC)}(\omega) = -\frac{(\omega_{p,j}^*)^2}{\omega(\omega + i\gamma_{p,j})}, \tag{3}$$

with

$$\omega_{p,j}^* = e\sqrt{\frac{N}{\varepsilon_0 m_j}}. \tag{4}$$

The unscreened plasma frequency $\omega^*_p$ depends on the free-charge-carrier concentration $N$ and the major elements along

the principle crystal axes of the effective conduction band mass, $m_j$ ($\varepsilon_0$ is the vacuum permittivity, and $e$ is the electrical unit charge). The plasmon broadening parameter $\gamma_p$ is related to the optical free-carrier mobility $\mu$:

$$\gamma_{p,j} = \frac{e}{m_j \mu_j}. \tag{5}$$

In a magnetic field the Drude contribution is now a tensor in the laboratory Cartesian coordinates ($x$,$y$,$z$) [23], [24]:

$$\varepsilon^{(FC-MO)}(\omega) = -\left\langle \omega_p^{*2} \right\rangle \left(\omega^2 I + i\omega\gamma\right)^{-1} + \tag{6}$$
$$+i \left\langle \omega_p^{*2} \right\rangle \omega \left\langle \omega_c \right\rangle \begin{pmatrix} 0 & -h_z & h_y \\ h_z & 0 & -h_x \\ -h_y & h_x & 0 \end{pmatrix}^{-1},$$

where $\left\langle \omega_p^{*2} \right\rangle$ may be defined as the (unscreened) "plasma frequency" tensor. The tensor leading the antisymmetric magnetic field contribution in Eq. 6 may be termed cyclotron frequency tensor

$$\left\langle \omega_c \right\rangle \equiv q \left(\frac{\mu_0 H}{m_0}\right) m^{-1}, \tag{7}$$

which depends on the magnitude $H$ of the magnetic field, the inverse effective free-charge-carrier mass tensor, and the free-charge-carrier type. As can be seen from $\varepsilon^{(FC-MO)}$, the magnetic field causes symmetry breaking in $\varepsilon$. For $H$ = 0, Eq. 6 is identical with Eq. 3. In Eq. 6 the magnetic field contribution scales with the inverse effective mass tensor $m^{-1}$. Therefore, if the magnetic-field induced changes in the dielectric function tensor can be determined, information on the effective mass tensor elements can be obtained.

## III. Results and Discussion

### A. Optical Hall effect in c-plane InN

Figures 1 and 2 show experimental and best-model calculated IRSE $\Psi$ and MOGE Mueller Matrix element $M_{ij}$ spectra, respectively. The analysis of the field-free IRSE data [28], [34] (Fig. 1) provides the phonon mode parameters [35]. It further renders, through the plasma frequency and broadening parameters, the coupled quantities $N/m$ and $N\mu$, where $N$, $\mu$ and $m$ are the free-carrier density, mobility and effective mass, respectively. Resonance structures in the IRSE spectra identify the InN $E_1$ (478 cm$^{-1}$) and $A_1$ TO phonons (443 cm$^{-1}$) and the LO phonon-plasmon coupled modes (LPP) (650-1000 cm$^{-1}$) in InN (Fig. 1). The resonance structures in Fig. 2 (at ~360 cm$^{-1}$ and ~450 cm$^{-1}$) originate from interface polariton excitations controlled by substrate phonon frequencies and the InN free carrier properties. Due to the magnetic field the polariton resonances split into left and right polarized modes which reflect differently off the surface, and hence the Mueller matrix elements reveal non-zero intensities. The InN interface polaritons provide access to the plasma and cyclotron frequencies and the plasmon damping parameter (see Eq. 7 and Ref. [23] for details), which makes possible to differentiate between $N$, $\mu$ and $m$ and to obtain the sign of the free-charge carriers. Note that

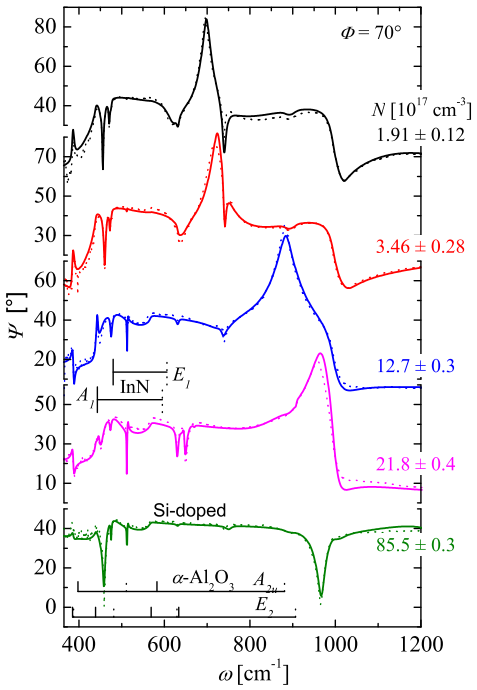


Fig. 1. Field-free ($\mu_0 H = 0$) experimental (dotted lines) and best-model (solid lines) IRSE $\Psi$ spectra [28].

in contrast to cyclotron resonance measurement there is no requirement on the plasmon damping to be smaller compared to the cyclotron frequency to create measurable polarization effects in the MOGE experiment.

As a result of a robust analysis of the combined IRSE and MOGE data (Figs. 1 and 2) two InN layers with different free electron properties and their dielectric function contributions have been unambiguously identified for all samples [28], [34]. The InN films were found to consist of a surface accumulation layer (thickness $d_s$) with a high electron density and a bulk layer (thickness $d$) with a lower electron density in accordance with the well established view [9], [11], [36], [37]. The zero-field IRSE data are very sensitive to the surface electron properties, which is exemplified in Fig. 3 for one of the InN films with intermediate bulk electron density. Figure 3 shows experimental and best model calculated $\Psi$ spectra assuming different model values of the surface electron density, $N_s d_s$. The solid line shows the calculated spectrum using the best-match value of $N_s d_s$ = 1.5×10$^{14}$, while the rest show the results with different surface electron densities as indicated in Fig. 3. It is seen that assuming a surface electron density, different from the best-match value, results in a poor agreement between experiment and calculated spectra in a large spectral range. The MOGE data possess similar high sensitivity to the surface electron properties in the vicinity of the interface polariton resonances.

From analysis of the optical Hall effect we obtained thickness, $d$ (in a very good agreement with transmission electron results), phonon mode parameters, free electron density, $N_b$,

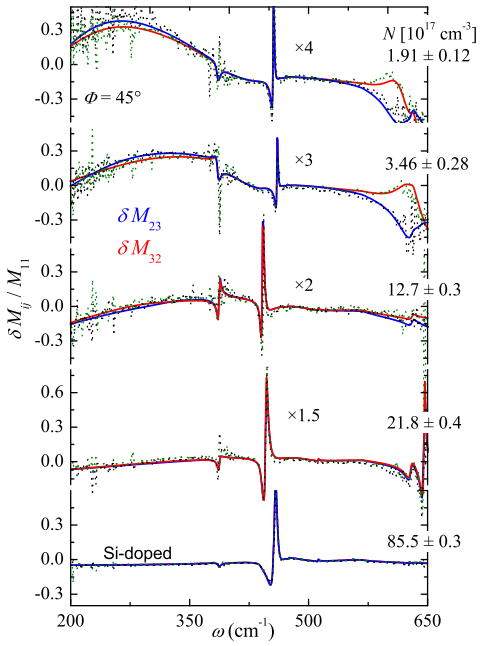


Fig. 2. Experimental (dotted lines) and best-model (solid lines) MOGE difference spectra $\delta M_{23}$, $\delta M_{32}$ taken between $M_{23}$, $M_{32}$ obtained at $\mu_0 H$ = -4.5T and $M_{23}$, $M_{32}$ at $\mu_0 H$ = +4.5T, respectively [28].

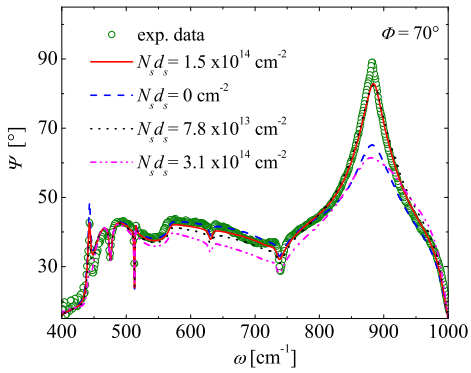


Fig. 3. Field-free ($\mu_0 H = 0$) experimental (dotted lines) and best model (lines) IRSE $\Psi$ spectra for the InN film with intermediate bulk electron density of $1.27\times10^{18}$ cm$^{-3}$ and different surface electron densities, $N_s d_s$. The solid (red) line indicates the calculated spectrum with the best-match calculated surface density value of $1.5\times10^{14}$ cm$^{-2}$.

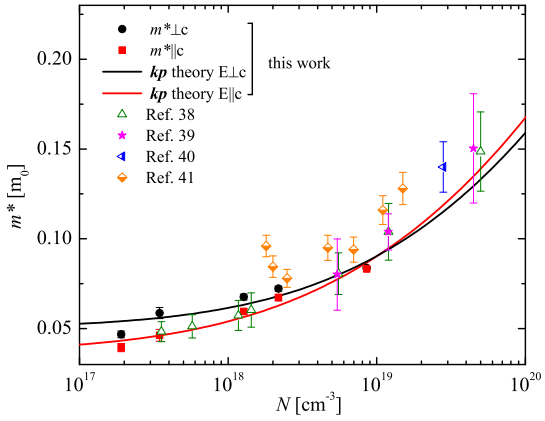


Fig. 4. Effective mass parameters of hexagonal InN for polarization parallel and perpendicular to the $c$-axis obtained from MOGE analysis [28]. Data from previous reports are included for comparison [38]–[41].

mobility, $\mu_j$, and effective mass, $m_j^*$ ($j$ denotes the polarization, being parallel or perpendicular to the **c**-axis), of the bulk InN and the surface electron density, $N_s d_s$ [28], [34]. The bulk electron mobility decreases linearly in double-log scale with increasing density from 1600 cm$^2$/(Vs) to 800 cm$^2$/(Vs), concordant with dominant ionized-impurity or donor-site scattering mechanism. We observe that $\mu_\parallel > \mu_\perp$, which we account for additional scattering across grain boundaries. Figure 4 depicts parallel and perpendicular electron effective mass parameters as a function of the bulk electron density. Previous data obtained from infrared studies and electrical Hall effect analysis are included for comparison [38]–[41]. We observe a significant anisotropy for $N < 10^{19}$ cm$^{-3}$. The out-of-plane mass $m_\perp^*$ is larger then $m_\parallel^*$. Kane's two-band **kp** model, upon comparison with the effective mass parameters obtained here for both polarizations, predicts for the bottom of the InN conduction band $m_\perp^\star$ = 0.050 $m_0$ and $m_\parallel^\star$ =0.037 $m_0$. These values are in excellent agreement with recent *ab initio* band-structure calculations [42]. Our observation quantitatively confirms the assumption of $m_\perp^* > m_\parallel^*$ concluded qualitatively from anomalous Shubnikov–de Haas oscillations in InN [43].

### *B. Bulk unintentional doping mechanism in c-plane InN*

Fig. 5 shows the bulk free-electron density, $N_b$, extracted from the optical Hall effect, as a function of the film thickness, $d$, for the unintentionally doped $c$-plane InN samples [34]. $N_b$ decreases with increasing thickness according to a power law $N_b \sim d^{-\alpha}$, with scaling factor $\alpha\approx1.8$. Free electron densities in unintentionally doped InN films obtained from electrical Hall effect were also reported decreasing with increasing film thickness [4], [5]. The apparent electrical Hall effect electron density was suggested as comprising a constant back-ground electron density (due to donor impurities), a fixed surface sheet density (due to the accumulation layer) and an electron density due to positively charged nitrogen vacancies associated with threading dislocations [4], [5]. The dependencies of the bulk electron density on film thickness according to Refs. [4], [5], which postulated a constant surface sheet density, are also shown in Fig. 5.

It is seen that the variation of the bulk free electron density in our InN films determined by the optical Hall effect does not follow the trends from Refs. [4] and [5]. In particular, the bulk electron densities of the InN films with thickness above 1 $\mu$m lie well below the density variation curves reported both in

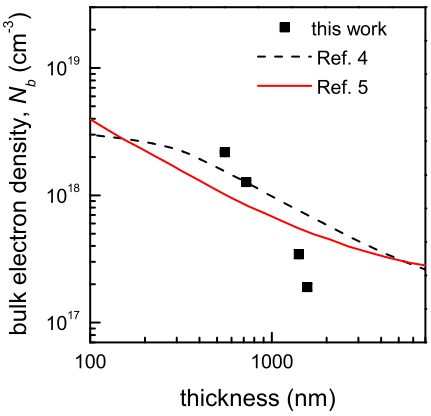


Fig. 5. Bulk free electron density, $N_b$, as a function of film thickness, $d$, determined by optical Hall effect [34].

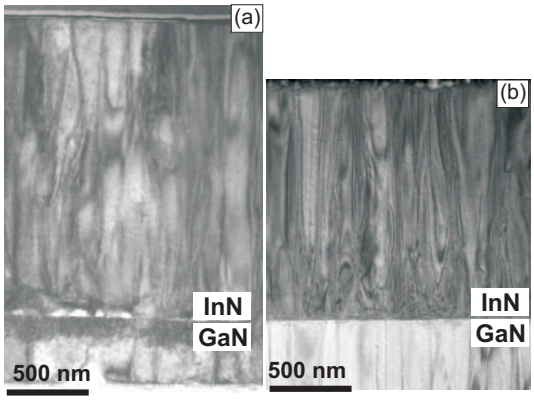


Fig. 6. Cross-section bright-field TEM image of the (a) 1.6 $\mu$m-thick InN film showing the lowest $N_b$=1.91×10$^{17}$ cm$^{-3}$ and (b) of an 1.3 $\mu$m-thick InN with a $N_b$=4.35×10$^{18}$ cm$^{-3}$.

Ref. [4] and in Ref. [5]. The origin of these differences may be traced back either to the variation of dislocation density with film thickness or/and the assumption of constant surface density used in the models of Refs. [4], [5]. First we consider the contribution of the dislocations to the free electron density in more details. Cimalla et al. [4] and Piper et al. [5] found that an exponential decay of dislocation density, associated with a density-independent mechanism of free electron generation, reproduces well the variation of electrical Hall electron density with InN thickness in a large number of samples grown at different conditions. However, it is obvious that the magnitude and variation of dislocation density with thickness are not universal but depend on the growth conditions, substrate and specific nucleation scheme used. For instance, it has been shown on the basis of x-ray diffraction measurements that the densities of both screw and edge type dislocations decrease with increasing the growth temperature [44]. Transmission electron microscopy (TEM) further gives rather scattered data: variations from 5×10$^{11}$ cm$^{-2}$ to 5×10$^{10}$ cm$^{-2}$ [4], and from 2.7×10$^{10}$ cm$^{-2}$ to 8.8×10$^{9}$ cm$^{-2}$ [45] over InN film thickness of ∼1 $\mu$m, and from 1.5×10$^{11}$ cm$^{-2}$ in the GaN buffer layer to 2.2×10$^{10}$ cm$^{-2}$ at the InN surface of a 0.76 $\mu$m thick InN film [36] have been reported.

To gain further insight into the variation of dislocation density with film thickness and its implications for the free electron behavior in InN we perform cross-section bright-field and dark field TEM. Figure 6 shows bright field TEM micrographs of the thickest (1.6 $\mu$m) InN film with the lowest bulk free-electron density of 1.91×10$^{17}$ cm$^{-3}$ (a) and a different 1.3 $\mu$m thick InN film with $N_b$ = 4.35×10$^{18}$ cm$^{-3}$ (grown by MBE on a metalorganic vapor phase epitaxial GaN buffer layer). These bright field images were recorded with the electron beam parallel to $\langle 11\bar{2}0\rangle$, which provides contrast with all present threading dislocations. A thin highly defective InN region (≈ 250 nm thick) can be seen at the interface with the GaN buffer layer for both samples [Figs. 6 (a) and (b)]. Individual defects in this interfacial region are hard to resolve unambiguously. Above the interfacial region the dislocation density is estimated to vary only marginally with film thickness, from 1.7±0.2×10$^{10}$ to 8.8±2.6×10$^{9}$ cm$^{-2}$ for the InN film in Fig. 6 (a) and from 3.1×10$^{10}$ to 2.4×10$^{10}$ cm$^{-2}$ for the InN film in Fig. 6 (b). This result is in agreement with previous findings that the major change in dislocation density in InN takes place within the substrate/buffer interfacial region of the InN film [36]. The above numbers for the dislocation density have also been confirmed by dark field imaging with different **g**-vectors.

Our findings further make evident that for certain growth conditions and nucleation schemes the variation of dislocation density with film thickness is much weaker than previously reported [4], [5]. We also measured, as discussed above, similar densities of dislocations in InN films with bulk electron densities that differ by more than an order of magnitude. Therefore, our TEM and optical Hall effect results (Figs. 5 and 6) indicate that the contribution of the dislocations to the thickness dependent doping mechanism might have been overestimated. Indeed, electrical Hall electron density in a 0.76 $\mu$m-thick InN film, grown on an yttrium-stabilized zirconium substrate, is in the range of 2-6×10$^{18}$ cm$^{-3}$ [46] and would require according to the models in Refs. [4], [5] a dislocation density of 1-5×10$^{10}$ cm$^{-2}$, which is at least an order of magnitude larger than the measured value of 1×10$^{9}$ cm$^{-2}$ [46]. Therefore, it is plausible to suggest that an additional thickness-dependent doping mechanism, unrelated to dislocations, must be invoked to explain the variation of the bulk free electron density with InN film thickness. Point defects, previously thought to be thickness independent are most likely the origin of this additional doping mechanism. Unintentional impurities, such as $O_N$, $Si_{In}$, $H_i$, and native defects, such as N vacancy and related complexes, are the obvious candidates. A combined glow discharge mass spectroscopy and electrical Hall effect measurement studies suggested that the high donor

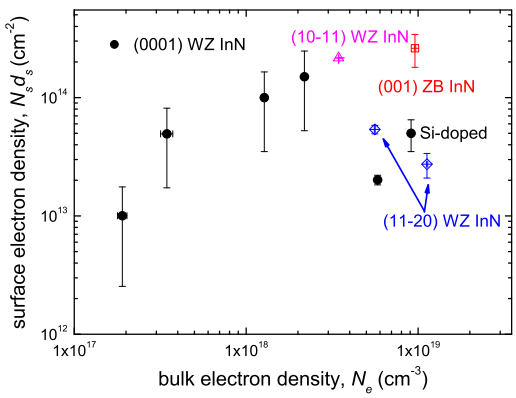


Fig. 7. Surface electron sheet density, $N_s d_s$, as a function of the bulk free electron density $N_b$ for WZ and ZB InN films with different surface orientations.

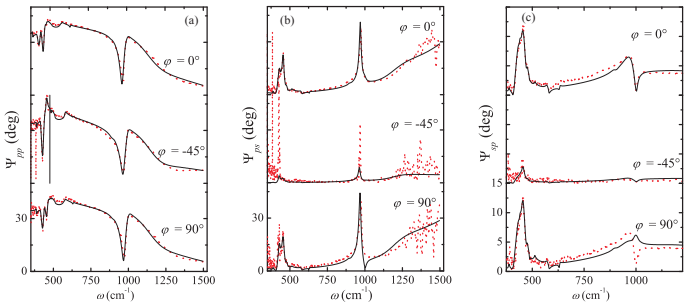


Fig. 8. Experimental (dots) and calculated (lines) GIRSE spectra of one representative (11$\bar{2}$0) InN film on *r*-plane sapphire for different angles $\varphi$ between the plane of incidence and the InN [0001] direction: (a) $\Psi_{pp}$, (b) $\Psi_{ps}$ and (c) $\Psi_{sp}$.

concentrations in unintentionally doped MBE InN could not be explained by O and Si, but possibly by H impurities [47]. Recent first-principles studies also suggested that monatomic hydrogen is the plausible cause of the unintentinal n-type conductivity in InN [6]. Both substitutional, $H_N^{2+}$, and interstitial hydrogen, $H_i^+$ were found to have lower formation energies than the positively charged nitrogen vacancy, which associated with dislocations was previously suggested to be the main donor responsible for the thickness dependence of free-electron density in InN films [4], [5]. Interestingly, $H_i^+$ has been estimated to be mobile at modest temperatures ($\geq$ 100 °C) [6], which can cause gradients in the free electron density with film thickness after cooling down from growth or processing temperatures. Hydrogen concentrations exceeding $10^{18}$ cm$^{-3}$ have been reported for MBE InN films [48].

### *C. Electron accumulation at polar, non-polar and semipolar WZ and (001) ZB InN surfaces*

The observed differences between our optical and the electrical Hall effect bulk electron densities (Fig. 5) may in addition originate from the assumption of a constant surface density used to extract the bulk electron density from the electrical measurements [4], [5]. We found that the surface sheet density determined by the optical Hall effect for the unintentionally doped *c*-plane InN films, $N_s d_s$, varies significantly with the bulk free electron density, $N_b$. The optical Hall effect $N_s d_s$ for the *c*-plane InN films are shown in Fig. 7 with filled circles. The *Si*- doped InN layer with $N_b$ of $9.1\times10^{18}$ cm$^{-3}$ is also included for comparison. The relatively larger errors (compared to the bulk densities) are due to the fact that the IRSE and MOGE data are sensitive to the surface sheet density, $N_s d_s$, rather than to the profile $N_s(t)$ ($0< t < d_s$) of the volumetric electron density within the thin surface accumulation layer. Nonetheless, a clear tendency of increasing surface sheet density with increasing bulk free electron density is seen.

It has been recognized that surface states which pin the Fermi level, $E_F$, tend to fall near a universal energy level known as the Fermi stabilization energy, $E_{FS}$ [3], [7]. $E_{FS}$ is located in the conduction band of InN, which causes the surface electron accumulation and was recently determined to lie at 1.83 eV above the valence band maximum (VBM) [49]. The surface Fermi level position was shown to increase with increasing the bulk electron density from $\sim$1.5 eV for an unintentionally doped InN with $N_b$=$2.0\times10^{18}$ cm$^{-3}$ to a saturation at $E_{FS}$ for heavily *Si*-doped InN with a $N_b$=$6.6\times10^{20}$ cm$^{-3}$ [49]. Therefore, we have adopted from Ref. [49] a pinning of the surface $E_F$ at 1.5 eV (1.64) above the VBM for our unintentionally doped (*Si*-doped) InN films when calculating the charge- and band-bending profiles [34]. The calculations were performed by solving Poisson's equation within the modified Thomas-Fermi approximation following Ref. [12] using a non-parabolic conduction band [50]. The shift of the conduction and valence band edges due to electron-electron, electron-hole, electron-impurity and hole-impurity interaction as a function of both electron and doping density have been included. The calculations showed a good agreement with the experimentally determined $N_s d_s$ for the *Si*-doped sample. On the other hand the calculated surface electron density in the unintentionally doped InN films increases marginally from $5.24\times10^{13}$ cm$^{-2}$ to $5.29\times10^{13}$ cm$^{-2}$ in contrast with the significant variation of $N_s d_s$ about one order of magnitude found experimentally (Fig. 7). The latter indicates a certain variation of the $E_F$ position at the surface of the unintentionally doped InN films with changing $N_b$. A presence of InN(000$\bar{1}$) inversion domains, shown to possess highly dispersive surface states [11] is among the possible explanations. However, at this stage the origin of the strong variation of $E_F$ at the InN surface remains unidentified.

We further studied the free electron behavior in WZ InN with semi-polar (10$\bar{1}$1) and non-polar (11$\bar{2}$0) surfaces, and ZB (001)-oriented InN film by GIRSE. Experimental and best-match calculated $\Psi$ spectra are shown in Fig. 8 for one representative non-polar InN sample. The dependence of the effective mass on the bulk electron density as determined by the optical Hall effect (see Fig. 4) was taken into account in the GIRSE modeling. From analysis of the GIRSE data the bulk

and surface electron density, and the mobilities of the non-polar and semipolar WZ InN, and (001) ZB InN films were determined. A distinct surface electron accumulation is found to occur at ZB (001)-, WZ ($11\bar{2}0$)-, and ($10\bar{1}1$) InN surfaces as shown in Fig. 7 by the open symbols. The presence of electron accumulation at the ZB (001)- and WZ ($11\bar{2}0$)-InN surfaces inferred by GIRSE in this work agrees with previous XPS findings that the surface Fermi level in such samples lies well above the CBM, indicating downward band bending at the surface, and thus surface electron accumulation [17].

We observe that the semi-polar ($10\bar{1}1$) surface behaves similarly to the polar surfaces in terms of surface charge (Fig. 7). On the other hand, $N_s d_s$ in the nonpolar InN films, are lower than the surface densities in undoped polar InN with similar bulk concentrations (Fig. 7). The surface densities at the nonpolar surfaces are however comparable to the surface density in polar Si-doped InN, but somehow larger than the surface density in *a*-plane InN inferred on the basis of combined XPS measurements and band structure calculations [17]. We note that any comparison shall be done with caution since the surface charge at non-polar surfaces is expected to be dependent on the growth conditions via different surface reconstructions [11]. Preliminary studies of our InN films indicate a different surface status even for films with the same surface orientations. Different surface chemistries might further complicate the picture since they play an important role for the surface band bending by partially neutralizing the surface donor-like states. For instance, oxidation of the InN surface has been shown to result in a decrease in the net free-electron density [51].

We measured by GIRSE an electron density at the ZB InN (001) surface of $1.14\pm0.31\times10^{14}$ cm$^{-2}$ (Fig. 7), more than an order of magnitude larger compared to the estimation in Ref. [17]. These differences may be related to the fact that our ZB InN film contains 25% of WZ InN domains with ($10\bar{1}1$) orientations. The later exhibit large electron accumulation at the surface (Fig. 7) and depending on the WZ domain distribution might lead to overestimation of $N_s d_s$ in our ZB InN sample. However, the observed differences may also be related to the atomic hydrogen cleaning at the surfaces prior to the XPS measurement [17], which may affect the surface chemistry and thus the electron density [52]. Further differences may arise due to the numerous assumptions when calculating the surface sheet density from the Poisson's equation within the modified Thomas-Fermi approximation.

## IV. Conclusion

We have demonstrated the disentanglement of bulk and surface accumulation electron densities in *c*-plane InN through the contactless optical Hall effect. It is shown that the variation of the bulk free electron density with film thickness does not follow the models accounting for a constant background electron density and free electrons from nitrogen vacancies along dislocations, proving the existence of an additional thickness-dependent doping mechanism. TEM studies showing a nearly constant density of dislocations above a thickness of 250 nm provide further support. Point defects, previously thought to be thickness independent are most likely the origin of this additional doping mechanism, and H impurities seem to be good candidate. The InN $\Gamma$-point effective mass is determined highly anisotropic $m^\star_\perp = 0.050 \pm 0.003\ m_0$ and $m^\star_\parallel = 0.037 \pm 0.003\ m_0$ for polarization perpendicular and parallel to the *c*-axis, respectively. The surface electron density in unintentionally doped *c*-plane InN is shown to decrease with decreasing bulk electron density. Further, we found that surface electron accumulation occurs not only at (0001) but also at WZ non-polar ($11\bar{2}0$) and semi-polar ($1\bar{1}01$) and (001) ZB InN surfaces showing complex behavior with bulk density. While the exact mechanisms behind these effects are still to be found, the possibility to tune surface charge density has significant implications for the design and realization of electronic and optoelectronic devices using InN.

## Acknowledgment

The Swedish Research Council (VR, under contract 2005-5054) and FCT Portugal (program Ciência 2007) are acknowledged for financial support. Part of the work is supported by NSF in MRSEC QSPIN at UNL, NSF-ECCS-824920, by US Army Research Office, and J. A. Woollam Foundation.

## References

[1] E. F. Schubert, *Light-emitting diodes*. Cambridge, U.K.: Cambridge University Press, 2003.
[2] L. Hsu and W. Walukiewicz, *J. Appl. Phys.*, vol. 104, p. 024507, 2008.
[3] W. Walukiewicz, *Physica B*, vol. 302, p. 123, 2001.
[4] V. Cimalla, V. Lebedev, F. M. Morales, R. Goldhahn, and O. Ambacher, *Appl. Phys. Lett.*, vol. 89, p. 172109, 2006.
[5] L. F. J. Piper, T. D. Veal, C. F. McConville, H. Lu, and W. J. Schaff, *Appl. Phys. Lett.*, vol. 88, p. 252109, 2006.
[6] A. Janotti and C. G. V. de Walle, *Appl. Phys. Lett.*, vol. 92, p. 032104, 2008.
[7] R. E. Jones, K. M. Yu, S. X. Li, W. Walukiewicz, J. W. Ager, E. E. Haller, H. Lu, and W. J. Schaff, *Phys. Rev. Lett.*, vol. 96, p. 125505, 2006.
[8] P. A. Anderson, C. H. Swartz, D. Carder, R. J. Reeves, S. M. Durbin, S. Chandril, and T. H. Myers, *Appl. Phys. Lett.*, vol. 89, p. 184104, 2006.
[9] I. Mahboob, T. D. Veal, C. F. McConville, H. Lu, and W. J. Schaff, *Phys. Rev. Lett.*, vol. 92, p. 036804, 2004.
[10] I. Mahboob, T. D. Veal, C. F. McConville, H. Lu, W. J. Schaf, J. Furthmüller, and F. Bechstedt, *Phys. Rev. B*, vol. 69, p. 201307, 2004.
[11] C. G. V. de Walle and D. Segev, *J. Appl. Phys.*, vol. 101, p. 081704, 2007.
[12] T. D. Veal, L. F. J. Piper, C. F. McConville, H. Lu, and W. J. Schaff, *J. Cryst. Growth*, vol. 288, p. 268, 2006.
[13] S. X. Li, K. M. Yu, R. E. Jones, W. Walukiewicz, J. W. Ager, W. Shan, E. E. Haller, H. Lu, and W. J. Schaff, *Phys. Rev. B*, vol. 71, p. 161201, 2005.
[14] P. Waltereit, O. Brandt, A. Trampert, H. Grahn, J. Menniger, M. Ramsteiner, M. Reiche, and K. H. Ploog, *Nature*, vol. 406, p. 865, 2000.
[15] M. McLaurin, T. E. Mates, and J. S. Speck, *Appl. Phys. Lett.*, vol. 86, p. 262104, 2005.
[16] P. Misra, U. Behn, O. Brandt, H. T. Grahn, B. Imer, S. Nakamura, S. P. DenBaars, and J. S. Speck, *Appl. Phys. Lett.*, vol. 88, p. 161920, 2006.
[17] P. D. C. King, T. D. Veal, P. H. Jefferson, C. F. McConville, F. Fuchs, J. Furthmüller, F. Bechstedt, P. Schley, R. Goldhahn, J. Schörmann, D. J. As, K. Lischka, D. Muto, H. Naoi, Y. Nanishi, H. Lu, and W. J. Schaf, *Appl. Phys. Lett.*, vol. 91, p. 092101, 2007.
[18] S. Lasiç, E. Gallardo, J. M. Calleja, F. Agulló-Rueda, J. Grandal, M. A. Sánchez-García, E. Calleja, E. Luna, and A. Trampert, *Phys. Rev. B*, vol. 76, p. 205319, 2007.

[19] H. Lu, W. J. Schaff, J. Hwang, H. Wu, G. Koley, and L. F. Eastman, *Appl. Phys. Lett.*, vol. 79, p. 1489, 2001.
[20] C.-L. Hsiao, T.-W. Liu, C.-T. Wu, H.-C. Hsu, G.-M. Hsu, L.-C. Chen, W.-Y. Shiao, C. C. Yang, A. Gällström, P.-O. Holtz, C.-C. Chen, , and K.-H. Chen, *Appl. Phys. Lett.*, vol. 92, p. 111914, 2008.
[21] Y. Kumagai, A. Tsuyuguchi, H. Naoi, H. Na, and Y. Nanishi, *Phys. Stat. Sol. B*, vol. 243, p. 1468, 2006.
[22] V. Darakchieva, T. Paskova, P. Paskov, B. Monemar, N. Ashkenov, and M. Schubert, *J. Appl. Phys.*, vol. 97, p. 013537, 2005.
[23] M. Schubert, *Infrared Ellipsometry on semiconductor layer structures: Phonons, plasmons and polaritons*. New York: Springer, 2004, vol. 209.
[24] M. Schubert, T. Hofmann, and C. M. Herzinger, *J. Opt. Soc. Am. A*, vol. 20, p. 347, 2003.
[25] T. Hofmann, M. Schubert, C. M. Herzinger, and I. Pietzonka, *Appl. Phys. Lett.*, vol. 82, p. 3463, 2003.
[26] T. Hofmann, M. Schubert, G. Leibiger, and V. Gottschalch, *Appl. Phys. Lett.*, vol. 90, p. 182110, 2007.
[27] T. Hofmann, U. Schade, K. C. Agarwal, B. Daniel, C. Klingshirn, M. Hetterich, C. M. Herzinger, and M. Schubert, *Appl. Phys. Lett.*, vol. 88, p. 042105, 2006.
[28] T. Hofmann, V. Darakchieva, B. Monemar, H. Lu, W. J. Schaff, and M. Schubert, *J. Electron. Mater.*, vol. 37, p. 611, 2008.
[29] M. Schubert, "Theory and application of generalized ellipsometry," in *Handbook of Ellipsometry*, H. Thompkins and E. A. Irene, Eds. Highland Mills: William Andrew Publishing, 2004.
[30] V. Darakchieva, J. Birch, M. Schubert, T. Paskova, S. Tungasmita, G. Wagner, A. Kasic, and B. Monemar, *Phys. Rev. B*, vol. 70, p. 045411, 2004.
[31] V. Darakchieva, T. Paskova, M. Schubert, P. P. Paskov, H. Arwin, B. Monemar, D. Hommel, M. Heuken, J. Off, F. Scholz, B. A. Haskell, P. T. Fini, J. S. Speck, and S. Nakamura, *Phys. Rev. B*, vol. 75, p. 195217, 2007.
[32] V. Darakchieva, *Phys. Status Solidi A*, vol. 205, p. 905, 2008.
[33] M. Schubert, *Annalen der Physik*, vol. 15, pp. 480–497, 2006.
[34] V. Darakchieva, T. Hofmann, M. Schubert, B. E. Sernelius, B. Monemar, P. O. A. Persson, F. Giuliani, E. Alves, H. Lu, and W. J. Schaff, *Appl. Phys. Lett.*, vol. 94, 2009.
[35] V. Darakchieva, P. P. Paskov, E. Valcheva, T. Paskova, B. Monemar, M. Schubert, H. Lu, and W. J. Schaff, *Appl. Phys. Lett.*, vol. 84, p. 3636, 2004.
[36] H. Lu, W. J. Schaff, L. F. Eastman, and C. E. Stutz, *Appl. Phys. Lett.*, vol. 82, p. 1736, 2003.
[37] C. H. Swartz, R. P. Tompkins, N. C. Giles, T. H. Myers, H. Lu, W. J. Schaff, and L. F. Eastman, *J. Cryst. Growth*, vol. 269, p. 29, 2004.
[38] S. Fu and Y. Chen, *Appl. Phys. Lett.*, vol. 85, p. 1523, 2004.
[39] J. Wu, W. Walukiewicz, K. Yu, J. W. Ager, E. E. Haller, H. Lu, W. J. Schaff, Y. Saito, and Y. Nanishi, *Appl. Phys. Lett.*, vol. 80, p. 3967, 2002.
[40] A. Kasic, M. Schubert, Y. Soito, Y. Nanishi, and G. Wagner, *Phys. Rev. B*, vol. 65, p. 115206, 2002.
[41] T. Inushima, M. Higashiwaki, and T. Matsui, *Phys. Rev. B*, vol. 68, p. 235204, 2003.
[42] P. Rinke, M. Scheffler, A. Qteish, M. Winkelnkemper, D. Bimberg, and J. Neugebauer, *Appl. Phys. Lett.*, vol. 89, p. 161919, 2006.
[43] T. Inushima, M. Higashiwaki, T. Matsui, T. Takenobu, and M. Motokawa, *Phys. Rev. B*, vol. 72, p. 85210, 2005.
[44] X. Wang, S.-B. Che, Y. Ishitani, and A. Yoshikawa, *Appl. Phys. Lett.*, vol. 90, p. 151901, 2007.
[45] E. Dimakis, E. Iliopoulos, K. Tsagaraki, T. Kehagias, P. Komininou, and A. Georgakilas, *J. Appl. Phys.*, vol. 97, p. 113520, 2005.
[46] C. H. Swartz, S. M. Durbin, P. A. Anderson, D. Carder, R. J. Reeves, S. Chandril, T. H. Myers, V. J. Kennedy, and S. P. Ahrenkiel, *Phys. Status Solidi C*, vol. 5, p. 508, 2008.
[47] D. C. Look, H. Lu, W. J. Schaff, J. Jasinski, and Z. Liliental-Weber, *Appl. Phys. Lett.*, vol. 80, p. 258, 2002.
[48] C. S. Gillinat, G. Koblmüller, J. S. Brown, S. Bernardis, J. S. Speck, G. D. Chern, E. D. Readinger, H. Shen, and M. Wraback, *Appl. Phys. Lett.*, vol. 89, p. 032109, 2006.
[49] P. D. C. King, T. D. Veal, P. H. Jefferson, S. A. Hatfield, L. F. J. Piper, C. F. McConville, F. Fuchs, J. Furthmüller, F. Bechstedt, H. Lu, and W. J. Schaff, *Phys. Rev. B*, vol. 77, p. 045316, 2008.
[50] J. Wu, W. Walukiewicz, W. Shan, J. W. Ager, E. E. Haller, H. Lu, and W. J. Schaff, *Phys. Rev. B*, vol. 66, p. 201403, 2002.
[51] V. Lebedev, C. Y. Wang, V. Cimalla, S. Hauguth, T. Kups, M. Ali, G. Ecke, M. Himmerlich, S. Krischok, J. A. Schaefer, O. Ambacher, V. M. Polyakov, and F. Schwierz, *J. Appl. Phys.*, vol. 101, p. 123705, 2007.
[52] G. Pettinari, F. Masia, M. Capizzi, A. Polimeni, M. Losurdo, G. Bruno, T. H. Kim, S. Choi, A. Brown, V. Lebedev, V. Cimalla, and O. Ambacher, *Phys. Rev. B*, vol. 77, p. 125207, 2008.